

Facile fabrication of twisted MoS_2 bilayers by direct bonding

Yu-Tong Chen(陈雨彤), Jie-Ying Liu(刘杰英), Lan-Ying Zhou(周兰英), Hua Yu(余画), Tong Li(李童), Qing Guan(关清), Na Li(李娜), Yang Chai(柴扬), and Guang-Yu Zhang(张广宇)

Citation: Chin. Phys. B, 2026, 35 (**1**): 016803. DOI: 10.1088/1674-1056/ae1c23
http://cpb.iphy.ac.cn; http://iopscience.iop.org/cpb

What follows is a list of articles you may be interested in

In-plane optical anisotropy of two-dimensional VOCl single crystal with weak interlayer interaction

Ruijie Wang(王瑞洁), Qilong Cui(崔其龙), Wen Zhu(朱文), Yijie Niu(牛艺杰), Zhanfeng Liu(刘站锋), Lei Zhang(张雷), Xiaojun Wu(武晓君), Shuangming Chen(陈双明), and Li Song(宋礼)

Chin. Phys. B, 2022, 31 (**9**): 096802. DOI: 10.1088/1674-1056/ac7555

Selective linear etching of monolayer black phosphorus using electron beams

Yuhao Pan(潘宇浩), Bao Lei(雷宝), Jingsi Qiao(乔婧思), Zhixin Hu(胡智鑫), Wu Zhou(周武), Wei Ji(季威)

Chin. Phys. B, 2020, 29 (**8**): 086801. DOI: 10.1088/1674-1056/ab9438

Epitaxial fabrication of two-dimensional $TiTe_2$ monolayer on Au(111) substrate with Te as buffer layer

Zhipeng Song(宋志朋), Bao Lei(雷宝), Yun Cao(曹云), Jing Qi(戚竞), Hao Peng(彭浩), Qin Wang(汪琴), Li Huang(黄立), Hongliang Lu(路红亮), Xiao Lin(林晓), Ye-Liang Wang(王业亮), Shixuan Du(杜世萱), Hong-Jun Gao(高鸿钧)

Chin. Phys. B, 2019, 28 (**5**): 056801. DOI: 10.1088/1674-1056/28/5/056801

Light-matter interaction of 2D materials: Physics and device applications

Zi-Wei Li(李梓维), Yi-Han Hu(胡义涵), Yu Li(李瑜), Zhe-Yu Fang(方哲宇)

Chin. Phys. B, 2017, 26 (**3**): 036802. DOI: 10.1088/1674-1056/26/3/036802

Photodetecting and light-emitting devices based on two-dimensional materials

Yuanfang Yu(于远方), Feng Miao(缪峰), Jun He(何军), Zhenhua Ni(倪振华)

Chin. Phys. B, 2017, 26 (**3**): 036801. DOI: 10.1088/1674-1056/26/3/036801

RAPID COMMUNICATION

Facile fabrication of twisted MoS_2 bilayers by direct bonding

Yu-Tong Chen(陈雨彤)[1,2,†], Jie-Ying Liu(刘杰英)[2,†,‡], Lan-Ying Zhou(周兰英)[2], Hua Yu(余画)[2], Tong Li(李童)[2], Qing Guan(关清)[2,5], Na Li(李娜)[2], Yang Chai(柴扬)[1,§], and Guang-Yu Zhang(张广宇)[2,3,4,¶]

[1] *Department of Applied Physics, The Hong Kong Polytechnic University, Hong Kong* 999077, *China*
[2] *Songshan Lake Materials Laboratory, Dongguan* 523808, *China*
[3] *Beijing National Laboratory for Condensed Matter Physics and Institute of Physics, Chinese Academy of Sciences, Beijing* 100190, *China*
[4] *School of Physical Sciences, University of Chinese Academy of Sciences, Beijing* 100190, *China*
[5] *The School of Integrated Circuits, Sun Yat-sen University, Shenzhen* 518107, *China*

(Received 9 September 2025; revised manuscript received 28 October 2025; accepted manuscript online 6 November 2025)

When stacking two-dimensional (2D) materials with a lattice mismatch and/or a small twist, moiré superlattice emerges with fascinating electronic and optical properties. The fabrication of such stacked 2D materials usually requires multiple transfer and stack processes, assisted by a certain transfer medium which needs to be removed afterwards, and it is very challenging to maintain pristine and clean surfaces/interfaces for these stacked structures. In this work, we report a facile direct bonding method for fabrication of twisted MoS_2 bilayers with ultra-clean surfaces/interfaces. Novel interlayer interactions are revealed in the as-fabricated high-quality samples, leading to twist-angle related dispersion behavior of various Raman modes, such as layer breathing modes, shear modes and E_{2g} modes, as well as indirect bandgap excitons. Field-effect transistors (FETs) of twisted MoS_2 bilayers also exhibit angle-dependent performance, which could be attributed to the band structure evolution. This facile method holds significance for the future integration of pre-designed multilayer 2D materials and paves a way to explore underlying physical mechanisms and potential applications.

Keywords: two-dimensional (2D) materials, direct bonding, moiré superlattice, twistronics

PACS: 68.65.Cd, 81.07.–b, 78.67.Pt

DOI: 10.1088/1674-1056/ae1c23 **CSTR:** 32038.14.CPB.ae1c23

1. Introduction

Two-dimensional (2D) moiré superlattice has given rise to a cornucopia of new phenomena, such as twist angle correlated electron states,[1,2] moiré excitons[3–5] and moiré phonons.[6,7] The most well-known 2D moiré superlattice is the magic-angle twisted bilayer graphene (TBG) recently demonstrated by Cao *et al*.[1] Fabrication of high-quality moiré system with precise twist angles is essential for the study of many intriguing physics. Generally, the fabrication of twisted 2D homo/heterostructures includes two strategies: direct growth and artificial stacking. While the former is constrained by thermodynamic mechanisms, the constituent materials are limited and they currently lack the capability for twist-angle control.[8–10] The latter applies to many different 2D materials and allows precise twist-angle control; but polymer supporting layers are usually involved during the transfer process, then contaminations such as polymer residues are inevitably present.[11–17]

Recently, we demonstrated a direct wafer bonding method to realize wafer-scale stacked 2D homo/heterostructures without any involvement of polymer or chemical solution.[18] However, wafer-to-wafer alignment for precise twist-angle control remains an unsolved challenge and twist-angle dependent properties remain unaddressed for as-fabricated 2D homo/heterostructures. In this work, we report a direct bonding of single-crystalline monolayer MoS_2 with hundred-micron domain sizes for twisted bilayers. A pre-alignment solution to the previous direct bonding method is developed, enabling twist angle control at a precision of $\pm 0.2^\circ$. The as-fabricated twisted bilayer MoS_2 (tb-MoS_2) features ultra-clean and flat surface/interface, large-scale homogeneity, and strong interlayer coupling. The Raman fingerprint reveals the crystallographic reconstruction at small twist angles as well as engineering of indirect bandgap. The electrical measurements show an anomalously high mobility at the twist angle of 59.1°, which relates to the emergence of flat band in large moiré superlattice near 60°. This new fabrication method offers distinct advantages in the fabrication of precisely angular-controllable twisted homo/heterostructures, exhibiting unique optical evolution and electronic states.

[†] These authors contributed equally to this work.
[‡] Corresponding author. E-mail: jyliu@iphy.ac.cn
[§] Corresponding author. E-mail: ychai@polyu.edu.hk
[¶] Corresponding author. E-mail: gyzhang@iphy.ac.cn

© 2026 Chinese Physical Society and IOP Publishing Ltd. All rights, including for text and data mining, AI training, and similar technologies, are reserved.

2. Method

The monolayer MoS_2 we use is grown on sapphire substrate via oxygen-assisted chemical vapor deposition (O-CVD) as described in our previous works.[19,20] Controlling the growth time enables the growth of triangular large-grain monolayer MoS_2 samples. The bonding process is performed in a glove box with water/oxygen concentration lower than 0.1 ppm. The bonding is conducted in a homemade apparatus, consisting of upper/lower flat plates. In the equipment, the hydraulic pressure module provides precise press force control (0–50000 N), and the temperature module controls the temperatures (20–500 °C) of both the upper and lower plates. During the bonding process, the temperature and pressure for both plates are 180 °C and ∼ 30 MPa, respectively. After pressure release, the bonded pair delaminates spontaneously, leaving as-fabricated tb-MoS_2.

To characterize the fabricated samples, Raman measurement is conducted on a Horiba LabRAM HR evolution Raman system with a 532 nm laser excitation. An 1800 lines/mm grating is used, providing a resolution of ∼ 0.7 cm^{-1}. An ultra-low frequency (ULF) module is added for Raman measurements below 50 cm^{-1}. The Raman spectrum is collected at 300 K in ambient atmosphere, and the photoluminescence (PL) spectrum at 300 K (78 K) is collected in ambient atmosphere (nitrogen atmosphere). Atomic force microscope (AFM) and piezoelectric force microscopy (PFM) imaging are performed by Bruker multimode 8 and Asylum cypher, respectively. Atomic-resolution high-angle annular dark-field (HAADF) scanning transmission electron microscope (STEM) images are acquired by the aberration-corrected JEM-ARM300F2 TEM operating at 300 kV.

As for the fabrication of FET devices, the tb-MoS_2 samples are transferred onto 20 nm Al_2O_3 dielectric layer via wet transfer method. After a standard ultraviolet (UV)-lithography patterning process, Au/Ti/Au electrodes are evaporated via an electron beam. Finally, the tb-MoS_2 is patterned into ribbon channels by UV-lithography and plasma etching. The electrical measurement is conducted in a Janis 4-probe station by an Agilent B1500 semiconductor parameter analyzer.

3. Results

3.1. Fabrication of tb-MoS_2 with precise twist angle control

Figure 1(a) illustrates the entire process including two steps: 1) pre-alignment and 2) direct bonding. The constituent MoS_2 are triangular large-grain monolayer MoS_2 grown on double-side polished (DSP) sapphire substrates (Fig. S1) by O-CVD. The triangular shape allows for orientation measurements under optical microscope during alignments, and transparent DSP sapphire enables a clear visualization when samples are viewed from its backside. The pre-alignment is realized using a transfer stage for precise twist-angle control. First, the back side of as-grown MoS_2/sapphire samples are adhered onto the center of two bare sapphire wafers via transparent adhesive (Bisphenol-A polycarbonate, PC). The bottom sapphire base is fixed on the rotatable bottom stage, while the upper sapphire base is attached to the upper stage with a transparent polydimethylsiloxane (PDMS) film supported by a glass slide. Figure 1(b) shows the optical microscope image of upper (dotted yellow line) and lower (dotted dark-blue line) MoS_2 triangles with a preset twist angle of 56.8°. After alignment, the glue (carbon tapes) that pre-adhered around the MoS_2 pieces are brought into contact, fixing the sapphire pair. The PDMS film detaches from the upper sapphire base and then starts the bonding process.

A typical as-fabricated tb-MoS_2 sample is shown in Fig. 1(c) with the twist angle of 56.68° (the angle deviation δ ∼ 0.12°). More tb-MoS_2 samples are shown in Fig. S2 and all the angle deviations are within 0.2°. In Table S1, we summarize angle deviations of typical transfer methods from previous results,[1,12,13,17,21,22] one can see that our method features one of the best alignment accuracies with considerably large size. These results reveal the effective angle control of our pre-alignment method. The holes and cracks in some samples are attributed to identical adhesion forces between two MoS_2 films and their growth substrates. As shown in Fig. S3(a), the bonded pair includes three interfaces: two MoS_2–sapphire interfaces and one MoS_2–MoS_2 interface. During debonding, the interface with the weakest adhesion forces delaminates. For bonding that uses two identical MoS_2 films, i.e., $f_{L1-substrate1} \approx f_{L2-substrate2}$, as shown in Fig. S3(b), the competition between two identical adhesion forces leads to fragment of bonded bilayer MoS_2 (Fig. S3(d)). This issue can be addressed by choosing samples with significant difference in adhesion forces (Fig. S3(c)), the resulting sample in Fig. S3(e) shows complete transfer of the overlapped MoS_2 area.

3.2. High-quality nature of as-fabricated tb-MoS_2

Using this method, we fabricate a series of high-quality tb-MoS_2 (Fig. S4), and the ultra-clean surfaces/interfaces are confirmed as follows. In a typical AFM image (Fig. 1(d)), the surface roughness is 0.047 nm, much flatter than that of samples fabricated by wet transfer method (0.519 nm) and pick-up dry transfer method (1.33 nm) as shown in Fig. S5. The clean interface leads to a strong interlayer coupling, as demonstrated by moiré patterns (Fig. S6) imaged by the PFM.[23] The moiré superlattice [24] in plane-view STEM images (Figs. S7 and S8) and interlayer spacing of 6.19 Å (close to the value in bulk MoS_2) in cross-section (Fig. S9) HAADF-STEM image further provide direct evidence for strong-coupling in our samples.

To further study the effect of interlayer coupling, we acquire Raman spectra on a 59.6° tb-MoS_2 sample shown in Figs. 2(a) and 2(b). Two strong low-frequency interlayer vibration modes, i.e., layer breathing mode (LB) and shear mode (S), appear in Fig. 2(a), indicating a great interlayer coupling. These modes are fingerprints of well-coupled moiré superlattice and are sensitive to twist angles.[25] Figure 2(c) exhibits the corresponding spatial mapping of frequency and intensity of LB and S modes, respectively. The uniform distribution indicates large-scale homogeneity and twist-angle uniformity in our samples. The spatial mapping images of E_{2g} and A_{1g} mode from as-fabricated tb-MoS_2 and as-grown 1L MoS_2 are shown in Fig. S10, also revealing the uniformity of our samples.

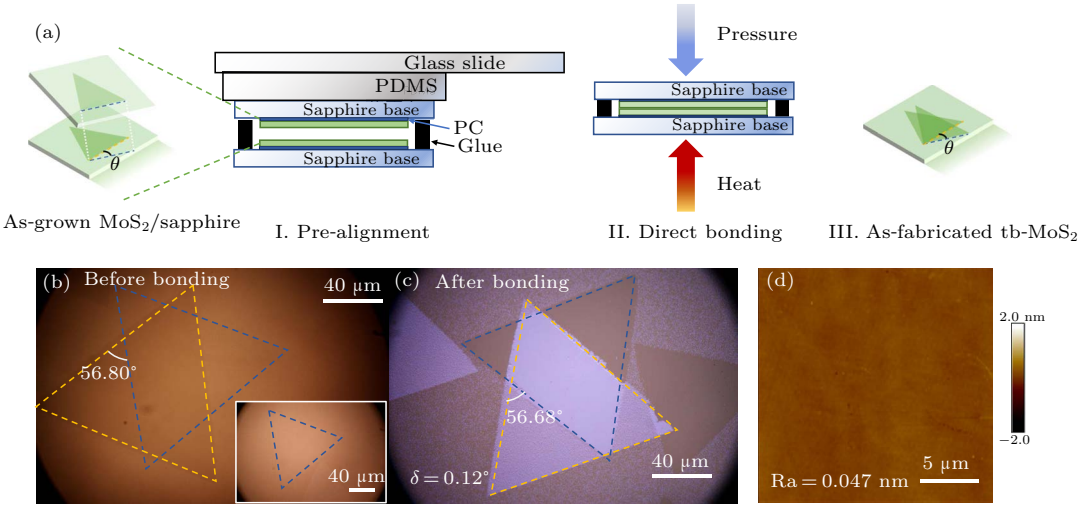


Fig. 1. Fabrication of bonded tb-MoS_2 with precise and controllable twist angles. (a) The schematic of pre-alignment and direct bonding process to obtain high-quality bilayer. (b) The optical images of monolayer MoS_2 prepared for pre-alignment, the yellow and dark-blue dotted lines outline the upper and lower triangles that artificially aligned to 56.80°. (c) The optical images of as-fabricated tb-MoS_2 after direct bonding and the obtained angle is measured as 56.68°. (d) The AFM image of as-obtained tb-MoS_2.

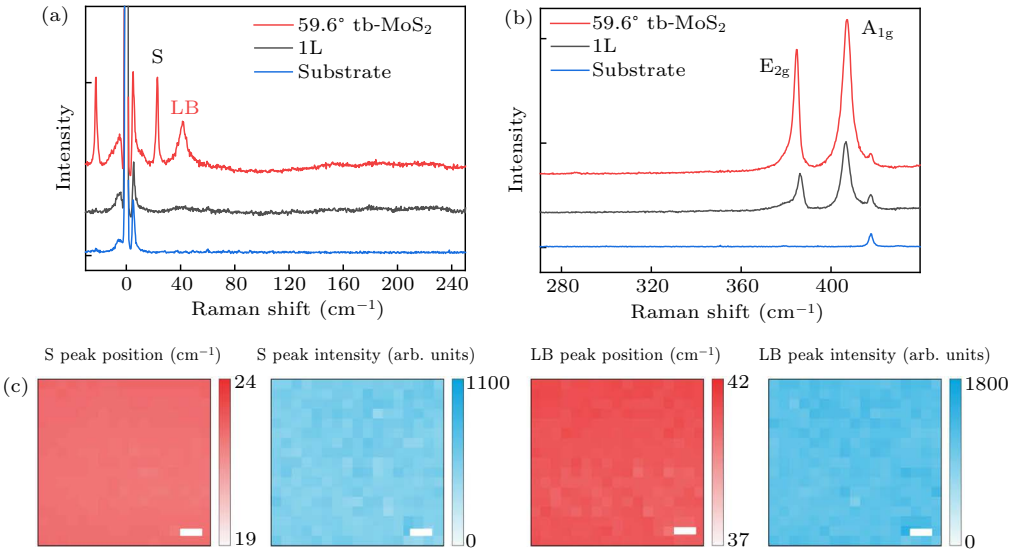


Fig. 2. Raman characterizations of as-fabricated tb-MoS_2 with strong interlayer coupling and great homogeneity. (a), (b) Comparison of Raman spectra of 59.6° tb-MoS_2, monolayer (1L), and substrate. (c) The peak position and intensity mapping images of shear (S) and layer breathing (LB) modes, the scale bar is 2 μm.

3.3. Twist-angle dependent properties in tb-MoS_2

In tb-MoS_2, the twist angle can engineer the atomic reconstruction, in-plane strain distribution and optical band structure,[26] which can be reflected via Raman spectra. The moiré phonons exhibited in Fig. 3(a) are folded acoustic phonons under the modulation of periodic moiré potentials,[7,27] and vary with the twist angles. The evolution of moiré phonon is determined by moiré period λ ($\lambda = a/[2\sin(\theta/2)]$, where a is the lattice constant of MoS_2). By calculating the phonon dispersion with respect to the reciprocal lattice vector $\boldsymbol{g}$[7,28–30] (see details in Fig. S11), we obtain the evolution of folded longitudinal acoustic (FLA) and folded transverse acoustic (FTA) as a function of the twist angle (calculated FLA and FTA in Fig. 3(c)). FLA and FTA extracted from Fig. 3(a) fit well with calculated results, demonstrating the high quality of our samples.

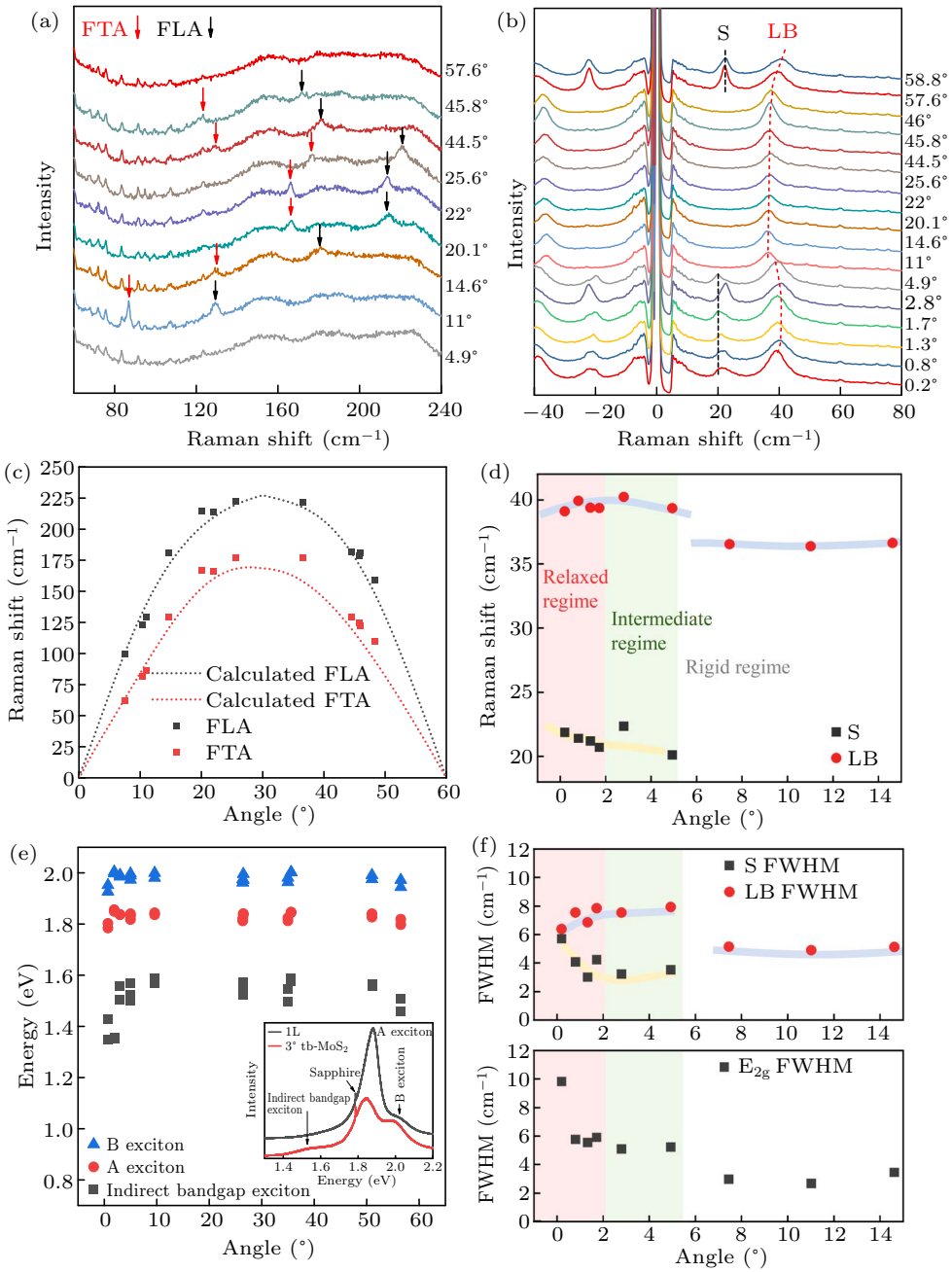


Fig. 3. Twist-angle dependent properties in tb-MoS_2. (a) Moiré phonons in tb-MoS_2 with different twist angles, marked by red arrows (FTA) and black arrows (FLA). (b) Low-frequency Raman spectra showing LB and S modes in tb-MoS_2 with different twist angles. (c) The calculated evolution of FTA (red dotted line) and FLA (black dotted line) with respect to twist angle, with the dots showing corresponding experimental results extracted from (a). (d) The θ-dependent evolution of Raman shifts of LB/S mode near 0°. The colored background indicates relaxed regime ($\theta < 2°$, pink), intermediate regime ($2 < \theta < 4.9°$, green) and rigid regime ($\theta > 4.9°$, white). (e) The θ-dependent evolution of A exciton, B exciton and indirect bandgap exciton. The inset exhibits PL spectrum of tb-MoS_2 and 1L MoS_2 at 300 K. (f) FWHM of LB/S mode (upper panel) and E_{2g} mode (bottom panel) near 0°.

Previous studies on tb-MoS_2 reveal a transition from rigid lattice to relaxed lattice when the twist angle decreases to near 0°.[23,31,32] This transition is also observed in our samples. As shown in Figs. 3(b) and 3(d), S mode appears and LB mode shows a sudden blue shift when twist angle θ is less than 4.9°. This phenomenon is attributed to the formation of reconstructed region that contributes to the emergence of the S mode with enhanced restoring force. These behaviors indicate the transition from rigid regime ($\theta > 4.9°$) to relaxed regime ($0 < \theta < 2°$).[31]

In the relaxed regime, the full width at half maximum (FWHM) of S mode (Fig. 3(f)) undergoes a rapid decrease from 0° to 2°, originating from the decreased in-plane strain that reduces the strain-induced splitting effect of the doubly degenerate S mode.[33] The reduced strain is also verified by similar behavior in the FWHM of E_{2g} mode (Fig. 3(f), the full spectra is shown in Fig. S12). In the relaxed regime, the moiré superlattice consists mainly of the $MX'/X'M$-stacking domains that are more energetically-favored,[31] verified by our PFM results of large $MX'/X'M$ domains. As the moiré period undergoes a large drop from 0° to 2° (Fig. S13), the $MX'/X'M$ domain area decreases, and the in-plane strain is

also modulated. When $\theta > 2°$, the moiré period is less than 10 nm, the strain among superlattice gradually becomes stable, and FWHM of S mode and E_{2g} remain unchanged,[31] referred to as the intermediate regime. As for LB mode, the FWHM increases as twist angle increases from 0° to 4.9° (Fig. 3(f)) along with a rapid frequency red shift at 4.9°, indicating a splitting here due to phonon-phonon coupling.[31] When $\theta > 4.9°$, the unchanged frequency and FWHM of LB mode indicate a stable rigid-superlattice.

PL spectrum also reveals the twist-angle dependent optical band structure (Figs. 3(e) and S14). As shown in the inset in Fig. 3(e), MoS_2 undergoes a transition from direct bandgap to indirect bandgap from monolayer to bilayer, with the appearance of indirect bandgap exciton. Figure 3(e) summarizes the positions of excitons as a function of the twist angle. Please also refer to Fig. S14 for low-temperature PL spectrum. The indirect bandgap exciton shows blue shift from 1.35 eV (∼ 0°) to 1.58 eV (∼ 30°), and shifts to 1.5 eV when the angle reaches higher; while the positions of A and B excitons remain nearly unchanged, in agreement with previous results.[13,34]

3.4. Electrical properties of tb-MoS_2

The electrical properties of tb-MoS_2 at different twist angles ranging from 0° to 60° are also investigated. The schematic device structure is shown in the inset in Fig. 4(a). The output curves (Fig. 4(a)) from a typical 59.1° tb-MoS_2 device exhibit linear behavior, suggesting an ohmic contact. Figure 4(b) shows the transfer curve from the same device and the on/off ratio reaches 10^7. The average field-effect mobility is summarized in Fig. 4(c), and it can be seen that the mobility slightly drops at around 10°/51.6° and reaches a maximum value of ∼ 50 $cm^2 \cdot V^{-1} \cdot s^{-1}$ at 59.1°. The high mobility near 60° can be attributed to high density of states from the flat electronic band.[35–37]

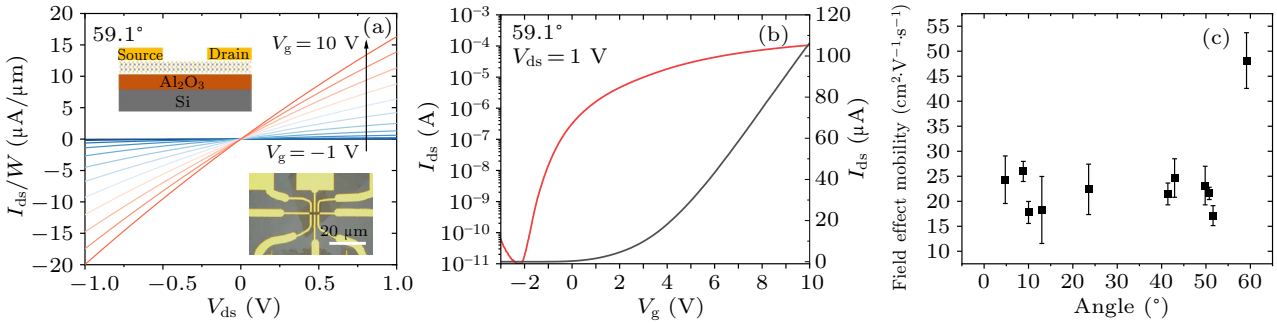


Fig. 4. The electrical properties of tb-MoS_2. (a) The output curve of the 59.1° tb-MoS_2. Inset: top left image exhibits schematic of a FET device, bottom right optical image shows the fabricated sample with the scale bar of 20 μm. (b) The electrical transfer curve of the 59.1° tb-MoS_2. (c) The twist-angle dependent mobility of tb-MoS_2, the error bar indicates the variations within the same angle.

4. Conclusion

We report a direct bonding method with precise angular alignment to fabricate large-scale, ultra-clean, uniform and high-quality tb-MoS_2 with a twist angle accuracy of 0.2°. In our as-fabricated samples, twist-angle dependent behavior of moiré phonons, interlayer vibration modes, and indirect bandgap are studied, revealing the evolution of superlattice, in-plane strain, as well as optical band structure. We also fabricate electrical devices with various twist angles and find signature of flat band near 60°. Our work provides a facile method to fabricate a moiré system and could pave a way for moiré physics and emerging applications.

Acknowledgements

This work is supported by Guangdong Major Project of Basic and Applied Basic Research (Grant No. 2021B0301030002), the National Key Research and Development Program (Grant No. 2021YFA1202900), and the National Natural Science Foundation of China (Grant Nos. 62204166 and 62404145).

References

[1] Cao Y, Fatemi V, Demir A, Fang S, Tomarken S L, Luo J Y, Sanchez-Yamagishi J D, Watanabe K, Taniguchi T, Kaxiras E, Ashoori R C and Jarillo-Herrero P 2018 *Nature* **556** 80
[2] Spanton E M, Zibrov A A, Zhou H, Taniguchi T, Watanabe K, Zaletel M P and Young A F 2018 *Science* **360** 62
[3] Tran K, Moody G, Wu F, Lu X, Choi J, Kim K, Rai A, Sanchez D A, Quan J, Singh A, Embley J, Zepeda A, Campbell M, Autry T, Taniguchi T, Watanabe K, Lu N, Banerjee S K, Silverman K L, Kim S, Tutuc E, Yang L, MacDonald A H and Li X 2019 *Nature* **567** 71
[4] Liu E, Barré E, Van Baren J, Wilson M, Taniguchi T, Watanabe K, Cui Y T, Gabor N M, Heinz T F, Chang Y C and Lui C H 2021 *Nature* **594** 46
[5] Seyler K L, Rivera P, Yu H, Wilson N P, Ray E L, Mandrus D G, Yan J, Yao W and Xu X 2019 *Nature* **567** 66
[6] Ramos-Alonso A, Remez B, Bennett D, Fernandes R M and Ochoa H 2025 *Phys. Rev. Lett.* **134** 026501
[7] Lin M L, Tan Q H, Wu J B, Chen X S, Wang J H, Pan Y H, Zhang X, Cong X, Zhang J, Ji W, Hu P A, Liu K H and Tan P H 2018 *ACS Nano* **12** 8770
[8] Zheng S, Sun L, Zhou X, Liu F, Liu Z, Shen Z and Fan H J 2015 *Adv. Opt. Mater.* **3** 1600
[9] Sun L, Wang Z, Wang Y, Zhao L, Li Y, Chen B, Huang S, Zhang S, Wang W, Pei D, Fang H, Zhong S, Liu H, Zhang J, Tong L, Chen Y, Li Z, Rümmeli M H, Novoselov K S, Peng H, Lin L and Liu Z 2021 *Nat. Commun.* **12** 2391
[10] Xu M, Ji H, Zheng L, Li W, Wang J, Wang H, Luo L, Lu Q, Gan X, Liu Z, Wang X and Huang W 2024 *Nat. Commun.* **15** 562
[11] Kang M A, Kim S J, Song W, Chang S, Park C Y, Myung S, Lim J, Lee S S and An K S 2017 *Carbon* **116** 167

[12] Mannix A J, Ye A, Sung S H, Ray A, Mujid F, Park C, Lee M, Kang J H, Shreiner R, High A A, Muller D A, Hovden R and Park J 2022 *Nat. Nanotechnol.* **17** 361

[13] Liao M, Wei Z, Du L, Wang Q, Tang J, Yu H, Wu F, Zhao J, Xu X, Han B, Liu K, Gao P, Polcar T, Sun Z, Shi D, Yang R and Zhang G 2020 *Nat. Commun.* **11** 2153

[14] Kim J H, Ko T J, Okogbue E, Han S S, Shawkat M S, Kaium M G, Oh K H, Chung H S and Jung Y 2019 *Sci. Rep.* **9** 1641

[15] Yun S J, Chae S H, Kim H, Park J C, Park J H, Han G H, Lee J S, Kim S M, Oh H M, Seok J, Jeong M S, Kim K K and Lee Y H 2015 *ACS Nano* **9** 5510

[16] Pizzocchero F, Gammelgaard L, Jessen B S, Caridad J M, Wang L, Hone J, Bøggild P and Booth T J 2016 *Nat. Commun.* **7** 11894

[17] Kim K, Yankowitz M, Fallahazad B, Kang S, Movva H C P, Huang S, Larentis S, Corbet C M, Taniguchi T, Watanabe K, Banerjee S K, Leroy B J and Tutuc E 2016 *Nano Lett.* **16** 1989

[18] Liu J, Zhao J, Li T, Ji D, Dai L, Li L,Wei Z, Li J,Wang Q, Yu H, Zhou L, Chen Y, Wu F, Zhu M, Sun H, Li Y, Zhang S, Tian J, Zhang X, Lu N, Bai X, Cao Z, Lin S, Wang S, Shi D, Li N, Du L, Yang W, Xian L and Zhang G 2025 *Nat. Electron.* **8** 1038

[19] Wang Q, Li N, Tang J, Zhu J, Zhang Q, Jia Q, Lu Y, Wei Z, Yu H, Zhao Y, Guo Y, Gu L, Sun G, Yang W, Yang R, Shi D and Zhang G 2020 *Nano Lett.* **20** 7193

[20] Li L, Wang Q, Wu F, Xu Q, Tian J, Huang Z, Wang Q, Zhao X, Zhang Q, Fan Q, Li X, Peng Y, Zhang Y, Ji K, Zhi A, Sun H, Zhu M, Zhu J, Lu N, Lu Y, Wang S, Bai X, Xu Y, Yang W, Li N, Shi D, Xian L, Liu K, Du L and Zhang G 2024 *Nat. Commun.* **15** 1825

[21] Zhang Y, Lee Y, Zhang W, Song D, Lee K, Zhao Y, Hao H, Zhao Z, Wang S, Kim K and Liu N 2023 *Adv. Funct. Mater.* **33** 2212210

[22] Wu K, Wang H, Yang M, Liu L, Sun Z, Hu G, Song Y, Han X, Guo J, Wu K, Feng B, Shen C, Huang Y, Shi Y, Cheng Z, Yang H, Bao L, Pantelides S T and Gao H J 2024 *Adv. Mater.* **36** 2313511

[23] McGilly L J, Kerelsky A, Finney N R, Shapovalov K, Shih E M, Ghiotto A, Zeng Y, Moore S L, Wu W, Bai Y, Watanabe K, Taniguchi T, Stengel M, Zhou L, Hone J, Zhu X, Basov D N, Dean C, Dreyer C E and Pasupathy A N 2020 *Nat. Nanotechnol.* **15** 580

[24] Weston A, Zou Y, Enaldiev V, Summerfield A, Clark N, Zólyomi V, Graham A, Yelgel C, Magorrian S, Zhou M, Zultak J, Hopkinson D, Barinov A, Bointon T H, Kretinin A, Wilson N R, Beton P H, Fal'ko V I, Haigh S J and Gorbachev R 2020 *Nat. Nanotechnol.* **15** 592

[25] Lin K, Holler J, Bauer J M, Parzefall P, Scheuck M, Peng B, Korn T, Bange S, Lupton J M and Schüller C 2021 *Adv. Mater.* **33** 2008333

[26] Du L, Molas M R, Huang Z, Zhang G, Wang F and Sun Z 2023 *Science* **379** 6639

[27] Lim S Y, Kim H, Choi Y W, Taniguchi T, Watanabe K, Choi H J and Cheong H 2023 *ACS Nano* **17** 13938

[28] Yankowitz M, Xue J, Cormode D, Sanchez-Yamagishi J D, Watanabe K, Taniguchi T, Jarillo-Herrero P, Jacquod P and Leroy B J 2012 *Nat. Phys.* **8** 382

[29] Lin M L, Tan Q H, Wu J Bin, Chen X S, Wang J H, Pan Y H, Zhang X, Cong X, Zhang J, Ji W, Hu P A, Liu K H and Tan P H 2018 *ACS Nano* **12** 8770

[30] Wu Y, Wang S, Chen C, Zhou C, Chen K, Zhou J, Wang Z, Bie Y and Deng S 2024 *Adv. Opt. Mater.* **12** 2301747

[31] Quan J, Linhart L, Lin M L, Lee D, Zhu J, Wang C Y, Hsu W T, Choi J, Embley J, Young C, Taniguchi T, Watanabe K, Shih C K, Lai K, MacDonald A H, Tan P H, Libisch F and Li X 2021 *Nat. Mater.* **20** 1100

[32] Weston A, Zou Y, Enaldiev V, Summerfield A, Clark N, Zólyomi V, Graham A, Yelgel C, Magorrian S, Zhou M, Zultak J, Hopkinson D, Barinov A, Bointon T H, Kretinin A, Wilson N R, Beton P H, Fal'ko V I, Haigh S J and Gorbachev R 2020 *Nat. Nanotechnol.* **15** 592

[33] Lee J U, Woo S, Park J, Park H C, Son Y W and Cheong H 2017 *Nat. Commun.* **8** 1370

[34] Liu K, Zhang L, Cao T, Jin C, Qiu D, Zhou Q, Zettl A, Yang P, Louie S G and Wang F 2014 *Nat. Commun.* **5** 4966

[35] Wu F, Xu Q, Wang Q, Chu Y, Li L, Tang J, Liu J, Tian J, Ji Y, Liu L, Yuan Y, Huang Z, Zhao J, Zan X, Watanabe K, Taniguchi T, Shi D, Gu G, Xu Y, Xian L, Yang W, Du L and Zhang G 2023 *Phys. Rev. Lett.* **131** 256201

[36] Xian L, Claassen M, Kiese D, Scherer M M, Trebst S, Kennes D M and Rubio A 2021 *Nat. Commun.* **12** 5644

[37] Naik M H and Jain M 2018 *Phys. Rev. Lett.* **121** 266401